RADIO AND X-RAY SHOCKS IN CLUSTERS OF GALAXIES

SUNGWOOK E. HONG[1], HYESUNG KANG[2], AND DONGSU RYU[3,4]

[1] School of Physics, Korea Institute for Advanced Study, Seoul 130-722, Korea; swhong@kias.re.kr
[2] Department of Earth Sciences, Pusan National University, Busan 609-735, Korea; hskang@pusan.ac.kr
[3] Department of Physics, UNIST, Ulsan 689-798, Korea; ryu@sirius.unist.ac.kr

ABSTRACT

Radio relics detected in the outskirts of galaxy clusters are thought to trace radio-emitting relativistic electrons accelerated at cosmological shocks. In this study, using the cosmological hydrodynamic simulation data for the large-scale structure formation and adopting a diffusive shock acceleration (DSA) model for the production of cosmic-ray (CR) electrons, we construct mock radio and X-ray maps of simulated galaxy clusters that are projected in the sky plane. Various properties of shocks and radio relics, including the shock Mach number, radio spectral index, and luminosity, are extracted from the synthetic maps and compared with observations. A substantial fraction of radio and X-ray shocks identified in these maps involve multiple shock surfaces along lines of sight (LOSs), and the morphology of shock distributions in the maps depends on the projection direction. Among multiple shocks in a given LOS, radio observations tend to pick up stronger shocks with flatter radio spectra, while X-ray observations preferentially select weaker shocks with larger kinetic energy flux. As a result, in some cases the shock Mach numbers and locations derived from radio and X-ray observations could differ from each other. We also find that the distributions of the spectral index and radio power of the synthetic radio relics are somewhat inconsistent with those of observed real relics; a bit more radio relics have been observed closer to the cluster core and with steeper spectral indices. We suggest that the inconsistency could be explained if very weak shocks with $M_s \lesssim 2$ accelerate CR electrons more efficiently, compared with the DSA model adopted here.

Key words: acceleration of particles – cosmic rays – galaxies: clusters: intracluster medium – methods: numerical – shock waves

1. INTRODUCTION

Since the discovery of a bow shock in the periphery of the bullet cluster 1E 0657-558 (Markevitch et al. 2002), it has been well established that shock waves exist in and around galaxy clusters. Using cosmological hydrodynamic simulations for the large-scale structure (LSS) formation of the universe, the origin and nature of shock waves in the intracluster medium (ICM) as well as in the intergalactic medium (IGM) have been extensively studied (Miniati et al. 2000; Ryu et al. 2003; Pfrommer et al. 2006; Kang et al. 2007; Hoeft et al. 2008; Skillman et al. 2008; Vazza et al. 2009). These studies have demonstrated that abundant shocks are produced by supersonic flow motions during the process of hierarchical clustering of nonlinear structures, and that they could be classified into two categories according to their locations relative to the host structures. *External shocks* are formed at the outermost surfaces surrounding clusters, filaments, and sheets of galaxies by the accretion of cool ($T \sim 10^3$–10^4 K), tenuous gas in voids onto those nonlinear structures. Because the accretion velocity around the clusters can be as high as $v_{\rm acc} \sim$ a few $\times 10^3$ km s^{-1} and the sound speed of accreting gas is $c_s \sim$ 5–15 km s^{-1}, external shocks are strong, with Mach numbers as large as $M_s \sim 10^3$. On the other hand, *internal shocks* are produced inside the nonlinear structures, where the gas has already been heated to high temperature by previous episodes of shock passage so that their Mach number is typically low, with $M_s \lesssim 10$. While most internal shocks have $M_s \lesssim 3$, those with $2 \lesssim M_s \lesssim 4$ play the most important role in dissipating the shock kinetic energy into heat in the ICM (e.g., Ryu et al. 2003; Kang et al. 2007).

Internal shocks could be further classified by their origins into a number of types that may not be mutually exclusive. *Turbulent shocks* are induced by turbulent flow motions in the ICM and they are expected to have very small Mach numbers, $M_s \lesssim 2$ (Porter et al. 2015). Turbulent motions in the ICM could be generated by several different processes: major or minor mergers, active galactic nucleus (AGN) jets, galactic winds, galaxy wakes, and so on (Subramanian et al. 2006; Ryu et al. 2008, 2012; Vazza et al. 2012b; Brunetti & Jones 2014). Bow shocks found in the outskirts of merging clusters are commonly referred to as *merger shocks* (Roettiger et al. 1999; Markevitch & Vikhlinin 2007; Skillman et al. 2013). In most cases, merger shocks are weak with $M_s \lesssim 3$ (e.g., Gabici & Blasi 2003). *Infall shocks* form by infall of the warm-hot intergalactic medium (WHIM; $T \sim 10^5$–10^7 K) into the hot ICM along adjacent filaments (Hong et al. 2014). They could have relatively high Mach numbers, reaching up to $M_s \sim 10$, and thus the ensuing cosmic-ray (CR) acceleration can be more efficient than in other types of shocks.

Including the shock in the bullet cluster, a number of shocks have been found in X-ray observations (e.g., Russell et al. 2010; Akamatsu et al. 2012; Ogrean & Brüggen 2013). In these observations, shocks are detected as sharp discontinuities in the temperature and surface brightness distributions, and their physical properties including the sonic Mach number, M_s, are estimated from the "deprojected" temperature and density jumps (Markevitch & Vikhlinin 2007). Most of the shocks detected in X-ray observations are weak with $M_s \sim 1.5$–3.

In addition, shocks in the ICM have been detected by radio observations, especially as so-called radio relics (see, e.g., Brüggen et al. 2012; Feretti et al. 2012, for reviews). Radio

---
[4] Author to whom any correspondence should be addressed.

relics are usually found in the cluster outskirts around the virial radius, r_{vir}. The radio emission is understood to be synchrotron radiation from CR electrons with the Lorentz factor of $\gamma_e \sim 10^3$–10^5, which are believed to be accelerated at the shocks associated with them (e.g., Ensslin et al. 1998; Bagchi et al. 2006; van Weeren et al. 2010). High energy nonthermal particles can be produced via diffusive shock acceleration (DSA) at astrophysical shocks, such as interplanetary and supernova remnant shocks as well as cluster shocks in collisionless tenuous plasma (Bell 1978; Blandford & Ostriker 1978; Drury 1983). Moreover, it has been shown that turbulence flow motions in the ICM can produce magnetic fields of up to $\sim \mu G$ level (e.g., Ryu et al. 2008).

Because the radio-emitting electrons with the Lorentz factor of $\gamma_e \sim 10^3$–10^5 would not advect or diffuse in the ICM more than ~ 100 kpc away from the shock surface before they lose the energy due to radiative cooling via synchrotron emission and inverse Compton (IC) scattering (e.g., Kang 2011), it is commonly thought that their acceleration sites are likely to be close to where the synchrotron emission is seen. Thus, the physical properties of shocks in radio relics are inferred from observed quantities such as the injection spectral index at the shock edge, $\alpha_{inj} = (M_s^2 + 3)/2(M_s^2 - 1)$, and the spatial profile of surface brightness (Drury 1983; Ensslin et al. 1998; Kang et al. 2012). Note that the spectral index for the synchrotron spectrum *integrated* over the downstream behind a steady planar shock is expected to be $\alpha \approx \alpha_{inj} + 0.5$ (e.g., Kang 2015a, 2015b; Kang & Ryu 2015). In most cases, the Mach number of shocks in radio relics was found to be in the range of $M_s \sim 1.5$–4.5 (e.g., Clarke & Ensslin 2006; Bonafede et al. 2009; van Weeren et al. 2010, 2012; Stroe et al. 2014b).

Pre-acceleration of thermal electrons to suprathermal energies and subsequent injection into the *Fermi* first-order process at shock has been an outstanding problem in the DSA theory. It is thought that the particle injection and DSA acceleration might be very inefficient at weak shocks ($M_s \lesssim 3$) because of small density compression across shocks (e.g., Malkov & Drury 2001). Especially in the so-called "thermal leakage" injection model, proton injection is expected to be strongly suppressed at weak shocks; the relative difference between postshock, proton thermal, and flow speeds is greater and so it is less likely for postshock protons to recross the shock front at weaker shocks (e.g., Kang et al. 2002). Although postshock electrons move faster than protons, they are more tightly tied to magnetic field fluctuations because of smaller rigidities (i.e., $p_{th,e} = (m_e/m_p)^{1/2} p_{th,p}$). Thus, it was also speculated that the DSA of electrons at weak shocks would not be efficient enough to explain the observed radio flux of the spectacular giant radio relics, such as the Sausage relic.

A pre-exiting population of electrons with the Lorentz factor of $\gamma_e \sim 10$–100 was suggested as a possible solution to the low electron injection problem at weak cluster shocks (Kang et al. 2012; Pinzke et al. 2013). Moreover, Kang et al. (2014) has suggested that a κ-like distribution of suprathermal electrons may exist in high beta ($\beta = P_g/P_B \sim 100$) ICM plasmas just like in solar winds, as well as facilitate the electron injection at weak shocks. Recently, Guo et al. (2014) and Park et al. (2015) used Particle-in-Cell (PIC) simulations of weak shocks in high beta plasmas to show that some of the incoming electrons gain energy via shock drift acceleration (SDA) and are reflected specularly toward the upstream region. Those reflected particles can be scattered back to the shock surface by plasma

waves excited in the upstream region, and then undergo multiple cycles of SDA, resulting in a power-law type suprathermal population up to $\gamma_e \sim 100$. These studies suggest a possibility that "self pre-acceleration" of thermal electrons to suprathermal energies via kinetic plasma processes at the shock itself might provide seed electrons enough to explain the observed flux level of bright radio relics.

The morphology of radio relics is, in some cases, observed to be elongated and arc-like with a sharp edge on one side. And some are found as a pair in the opposite side of clusters. So radio relics are often interpreted as products of binary mergers (e.g., Ensslin et al. 1998; Roettiger et al. 1999; van Weeren et al. 2010; de Gasperin et al. 2014). Several numerical studies have suggested that merger shocks with a sufficient amount of shock kinetic energy flux could produce radio relics (Nuza et al. 2012; Vazza et al. 2012a; Skillman et al. 2013). In these studies, synthetic radio maps were constructed by identifying shocks in simulated clusters and modeling CR electron injection/acceleration and magnetic field strength. However, there remain a few issues to be resolved before the simple picture of merger shocks being the origin of radio relics is accepted.

The first issue concerns the frequency of observed radio relics. Although structure-formation simulations have demonstrated that shocks are produced frequently during mergers and they should last for the cluster dynamical time of $t_{dyn} \sim 1$ Gyr, only about 10% of X-ray luminous clusters host some radio relics and putative merger shocks; the fraction of merging clusters with giant radio relics is much lower (Feretti et al. 2012). Recently, it has been suggested that ICM shocks may light up as radio relics only when they encounter fossil relativistic electrons that are leftover from either a previous episode of shock/turbulence acceleration or a radio jet from AGN (Kang & Ryu 2015; Shimwell et al. 2015). In this scenario, only a small faction of ICM shocks become radio-emitting structures for a fraction of the dynamical time ($\lesssim 0.1 t_{dyn} \sim 100$ Myr). Thus, the rareness of radio relics could be explained. Of course, this model can be justified only if the injection and acceleration of electrons at weak shocks in the ICM is very inefficient, which means the re-acceleration of pre-existing CR electrons must be required for the birth of radio relics.

The second issue involves the discrepancies in the shock properties inferred from radio and X-ray observations of a few radio relics. Among several dozens of observed radio relics, only a fraction of shocks associated with them have been detected in X-ray observations (Bonafede et al. 2012; Nuza et al. 2012, and references therein). In the case of the Toothbrush relic in 1RXS J0603.3, for exmaple, the radio index was measured to be $\alpha_{inj} \approx 0.6$–0.7, indicating a "radio Mach number," $M_{radio} \approx 3.3$–4.6 (van Weeren et al. 2012). But temperature and density discontinuities in X-ray observations suggest that an "X-ray Mach number," $M_X \lesssim 2$, and the position of the shock identified in X-ray observations is shifted from that in radio observations by $\gtrsim 200$ kpc (Akamatsu & Kawahara 2013; Ogrean et al. 2013). In addition, for the radio relic in A2256 Trasatti et al. (2015) suggested that if the observed index $\alpha_{63}^{1360} \approx 0.85$ measured between 63 and 1360 MHz is interpreted as the injection index, the radio Mach number can be estimated to be $M_{radio} \approx 2.6$, while the temperature jump measured in X-ray observations implies the X-ray Mach number, $M_X \sim 1.7$. In the case of the Sausage relic in CIZA J2242.8, van Weeren et al. (2010) used the observed

radio spectral index near the edge (shock surface), $\alpha_{\rm inj} \approx 0.6$, to obtain a radio-inferred shock Mach number, $M_{\rm radio} \approx 4.6$. However, the X-ray-inferred Mach number reported later by *Suzaku* and *Chandra* observations turned out to be lower, with $M_{\rm X\text{-}ray} \approx 2.54\text{–}3.15$ (Akamatsu & Kawahara 2013; Ogrean et al. 2014). Recently, Stroe et al. (2014a) estimated a steeper value, $\alpha_{\rm inj} \approx 0.77$, by performing a spatially resolved spectral fitting, implying a weaker shock with $M_{\rm radio} \approx 2.9$ that was in good agreement with X-ray observations.

In Hong et al. (2014, hereafter Paper I), we studied the properties of shock waves in the outskirts of simulated galaxy clusters using sets of LSS formation simulations. We find that in addition to merger shocks, infall shocks are produced in ICMs by continuous infall of density clumps (i.e., minor mergers) along filaments of galaxies to hot ICMs. Unlike weak bow shocks ($M_s \lesssim 2$) driven by major mergers, infall shocks do not show pairing structures and have higher Mach numbers ($M_s \sim 3\text{–}10$). In a few cases (e.g., Coma 1253+275 and NGC 1265), observed radio relics are thought to be associated with infall shocks (Brown & Rudnick 2011; Pfrommer & Jones 2011; Ogrean & Brüggen 2013).

In this paper, we consider a scenario in which suprathermal electrons are injected directly at the shocks without the help of fossil CR electrons, and are accelerated to radio-emitting energies. The frequency of radio relics depends on the shock statistics, while the radio luminosity of radio relics is determined by the shock kinetic energy flux and the assumed DSA efficiency model (e.g., Kang & Ryu 2013). In this scenario, the rareness of radio relics, compared to the frequency of the ICM shocks, can be controlled by adjusting the models for the DSA acceleration efficiency and the magnetic field amplification. For instance, Vazza et al. (2012a) used structure-formation simulations and generated mock radio maps of simulated cluster samples to show that radio emission tends to increase toward the cluster periphery and peak around $0.2\text{–}0.5 r_{\rm vir}$, mainly because the kinetic energy dissipated at shocks peaks around $0.2 R_{\rm vir}$ and the Mach number of shocks tends to increase toward the cluster outskirts. Such findings can explain why radio relics are rarely found in the cluster central regions.

We study the properties of radio and X-ray shocks in the simulated cluster sample of Paper I, based on a DSA model in which suprathermal electrons are injected and accelerated preferentially at shocks with higher Mach numbers. We first calculate synchrotron emission at shocks by modeling the primary CR electron population based on recent DSA simulations (Kang & Ryu 2013), as well as the magnetic field distribution based on a turbulent dynamo model (Ryu et al. 2008). We produce mock radio and X-ray maps by projecting the synchrotron and bremsstrahlung emission, respectively. We then identify "synthetic radio relics" in the radio map and extract their properties, such as radio and X-ray shock Mach numbers, $M_{\rm radio}$ and M_X, and their locations in the map. We examine the radio and X-ray properties of relic shocks, and attempt to understand the discrepancies derived from radio and X-ray observations in some radio relics.

In Section 2, we present numerical details such as the calculation of synchrotron emission at shock, the construction of mock radio and X-ray maps, and the extraction of radio and X-ray shock Mach numbers. In Section 3, we discuss how the two-dimensional (2D) projection of three-dimensional (3D) shock distributions affect the radio and X-ray observations of ICM shocks. In Section 4, we describe the properties of shocks

in the 2D projection as well as the properties for synthetic radio relics. Summary follows in Section 5.

2. NUMERICAL DETAILS

2.1. Clusters and Shocks

The construction of the galaxy cluster sample and the identification of shocks are described in detail in Paper I, so here they are summarized only briefly. The LSS formation simulations adopted a standard ΛCDM model with the following parameters: baryon density fraction $\Omega_{\rm BM} = 0.044$, dark matter density fraction $\Omega_{\rm DM} = 0.236$, cosmological constant fraction $\Omega_\Lambda = 0.72$, Hubble parameter $h \equiv H_0/(100\ {\rm km\ s}^{-1}\ {\rm Mpc}^{-1}) = 0.7$, rms density fluctuation $\sigma_8 = 0.82$, and the primordial spectral index $n = 0.96$. An updated version of a particle-mesh/Eulerian hydrodynamic code described in Ryu et al. (1993) was used for the simulations. Three sets of simulations were performed: (1) 16 different realizations of LSS formation in a comoving cubic box of $L = 100\ h^{-1}$ Mpc with 1024^3 uniform grid zones, (2) 16 different realizations in a comoving cubic box of $L = 200\ h^{-1}$ Mpc with 1024^3 zones, and (3) one realization in a comoving cubic box of $L = 100\ h^{-1}$ Mpc with 2048^3 zones. The sets of (1) and (2) were performed in an adiabatic (non-radiative) way, whereas (3) includes mild feedback from star formation and cooling/heating processes. In Paper I we find that the statistics of the physical properties of clusters and shocks are similar in all three types of simulations.

In the simulation data, clusters are identified as regions around local peaks in the spatial distribution of X-ray emissivity. Around each peak, the X-ray emission-weighted mean temperature, $T_{X,{\rm cl}}$, is obtained for the spherical volume within $r \leqslant r_{200}$. Here, $r_{200} \approx 1.3 r_{\rm vir}$ is the radius within which the gas overdensity is 200 times the mean gas density of the universe. Those with $k_{\rm B} T_{X,{\rm cl}} \geqslant 2\ {\rm keV}$ for $100\ h^{-1}$ Mpc box simulations and $k_{\rm B} T_{X,{\rm cl}} \geqslant 4\ {\rm keV}$ for $200\ h^{-1}$ Mpc box simulations are selected as synthetic clusters, resulting in a total of 228 clusters from the three sets of simulations. Here, $k_{\rm B}$ is the Boltzmann constant.

Shocks (actually, shock zones) are identified by a set of criteria given in Paper I, and their sonic Mach numbers, M_s, are estimated from the temperature jump condition, $T_2/T_1 = (5 M_s^2 - 1)(M_s^2 + 3)/(16 M_s^2)$, where T is the gas temperature. Hereafter, the subscripts "1" and "2" indicate the preshock and postshock quantities, respectively. Only shocks with $M_s \geqslant 1.5$ are considered. Note that a shock surface normally consists of many of these shock zones. The shock speed and shock kinetic energy flux at the shock zone are then calculated as $v_1 = M_s (\gamma P_{\rm th,1}/\rho_1)^{1/2}$ and $f_{\rm kin} = (1/2)\rho_1 v_1^3$, respectively, where $P_{\rm th,1}$ is the preshock thermal pressure and $\gamma = 5/3$ is the gas adiabatic index. The energy flux of CR protons can be estimated as

$$f_{\rm CR,p} = \eta(M_s) \cdot f_{\rm kin} = \eta(M_s) \cdot (1/2)\rho_1 v_1^3, \qquad (1)$$

where $\eta(M_s)$ is the CR acceleration efficiency via the DSA process. For the efficiency, the values presented in Kang & Ryu (2013; also shown in Figure 2 of Paper I) are adopted.

In Paper I, we find that the morphology of shock surfaces is quite complex due to the dynamic history of clusters, and in general a connected shock surface can consist of a number of grid zones of different types of shocks, including merger shocks (see Figure 7 in Paper I).

2.2. Modeling of Magnetic Field Strength

To calculate radio synchrotron emission at cluster shocks, we need to model the strength of magnetic fields as well as the energy spectrum of CR electrons. The ICM is observed to be permeated with the magnetic fields of a few μG in the cluster core region and a few $\times\ 0.1\ \mu$G in the cluster periphery (e.g., Bonafede et al. 2011; Feretti et al. 2012). Suggested ideas for the generation and amplification of magnetic fields in the ICM include processes during primordial phase transitions, Biermann battery mechanism, plasma processes at collisionless shocks, different types of turbulence dynamo, and the ejection of galactic winds and AGN jets (e.g., Dolag et al. 2008; Ryu et al. 2008, 2012; Widrow et al. 2012).

We adopt the turbulent dynamo model of Ryu et al. (2008), which assumes that turbulent flow motions are induced via stretching and compression of the vorticity generated behind the curved surfaces of shocks in clusters, and the magnetic fields are amplified by the turbulent flows. This allows the strength of the resulting magnetic fields to be modeled in terms of the number of local eddy turnover by the following fitting formula:

$$\frac{B^2}{8\pi\epsilon_{\text{turb}}} \equiv \phi(t/t_{\text{eddy}})$$
$$\approx \begin{cases} 0.04 \cdot \exp\left[\left(t/t_{\text{eddy}} - 4\right)/0.36\right] & \text{for } t/t_{\text{eddy}} < 4 \\ (0.36/41) \cdot \left(t/t_{\text{eddy}} - 4\right) + 0.04 & \text{for } t/t_{\text{eddy}} > 4 \end{cases},$$

where ϵ_{turb} is the turbulent energy density and $t_{\text{eddy}} \equiv 1/|\boldsymbol{\nabla} \times \boldsymbol{v}|$ is the reciprocal of the vorticity calculated from the local flow speed. The fitting function ϕ represents the fraction of the turbulent energy transferred to the magnetic energy via turbulent dynamo, and is derived from a magnetohydrodynamic simulation (Ryu et al. 2008). This model predicts that the magnetic field strength reaches a few μG in the cluster center and decreases to $\sim 0.1\ \mu$G toward the cluster outskirts. This is in a good agreement with the observed magnetic field strength in actual clusters (e.g., Carilli & Taylor 2002; Govoni & Feretti 2004; Bonafede et al. 2011).

2.3. Modeling of CR Electron Spectrum

For the energy spectrum of CR electrons, we first assume that the CR acceleration at shock is described by the test-particle model (Drury 1983), because most of the shocks found in clusters are weak (see introduction). Then, the momentum distribution of CR protons at the shock position can be described by the power-law form for $p \geqslant p_{\text{min}}$,

$$f_{\text{p}}(\tilde{p}) = f_{\text{p0}} \times \tilde{p}^{-q}, \qquad (3)$$

where $\tilde{p} \equiv p/(m_{\text{p}}c)$ is the dimensionless proton momentum, m_{p} is the proton mass, and $q = 3\sigma/(\sigma - 1)$ is the spectral index. The shock compression ratio is determined by the sonic Mach number to be $\sigma = (\gamma + 1)M_{\text{s}}^2/[(\gamma - 1)M_{\text{s}}^2 + 2]$. The normalization factor f_{p0} at each shock zone is determined by setting the CR energy flux through the shock zone to be

$$f_{\text{CR,p}} = v_2 \cdot m_{\text{p}}c^2 \int_{\tilde{p}_{\text{inj}}}^{\infty} \left(\sqrt{\tilde{p}^2 + 1} - 1\right) f_{\text{p}}(\tilde{p}) d\tilde{p}^3 \qquad (4)$$

where $v_2 = v_1/\sigma$ is the postshock flow speed and $f_{\text{CR,p}}$ is given in Equation (1). We do *not* consider the re-acceleration of pre-existing CRs in this work.

Here, $p_{\text{min}} = p_{\text{inj}}$ is the injection momentum above which particles can participate in the DSA process. According to recent PIC and hybrid simulations, both protons and electrons can initially gain energies via SDA while confined between the shock front and the preshock region by scatterings due to self-generated upstream waves (Guo et al. 2014; Caprioli et al. 2015; Park et al. 2015, see introduction). Particles should have a rigidity ($R = pc/e$) large enough to cross the shock front (i.e., $p_{\text{inj}} \sim 3p_{\text{th,p}} \sim 130p_{\text{th,e}}$,) in order to take part in the full first-order *Fermi* process. Here, $p_{\text{th,p}} = \sqrt{2m_{\text{p}}k_{\text{B}}T_2}$ is the most probable momentum of thermal protons of postshock gas with temperature T_2, while the most probable momentum of thermal electrons is $p_{\text{th,e}} = (m_{\text{e}}/m_{\text{p}})^{1/2}p_{\text{th,p}}$. In fact, p_{inj} is expected to depend on the shock Mach number, obliquity angle, and shock speed. For the sake of simplicity, we set $\tilde{p}_{\text{inj}} = 0.01$ in all shock zones regardless of the shock speed, Mach number, and ICM temperature.

Since the DSA process operates on CR protons and electrons with the same rigidity in the same manner, the momentum distribution of primary CR electrons at shocks should follow that of CR protons, except there will be less efficient injection and radiative cooling (e.g., Kang 2011; Park et al. 2015). The injection rate of CR electrons is expected be much lower than that of CR protons, because postshock thermal electrons need to be pre-accelerated from the thermal momentum to p_{inj} in order to get injected into the DSA process. Because the electron pre-acceleration is not yet fully constrained by plasma physics (despite recent PIC simulations, see introduction), it is often parameterized by the CR electron-to-proton ratio, $K_{\text{e/p}}$. Different types of observations have indicated a wide range of $K_{\text{e/p}} \sim 10^{-4}$–$10^{-2}$ (e.g., Schlickeiser 2002; Morlino et al. 2009), so we adopt the CR electron momentum distribution of $f_{\text{e}}(\tilde{p}) = K_{\text{e/p}} \cdot f_{\text{p}}(\tilde{p})$ for $p \geqslant p_{\text{min}}$ with $K_{\text{e/p}} \sim 0.01$. Adopting a higher value of $K_{\text{e/p}}$, as suggested by some recent PIC simulations (Guo et al. 2014; Caprioli et al. 2015), will increase the amplitude of $f_{\text{e}}(\tilde{p})$ and therefore the synchrotron radiation flux uniformly for all shocks.

While gaining energy via the DSA process at shock, CR electrons also lose energy via synchrotron emission and IC scattering. As a result, an equilibrium momentum exists, where the momentum gain is balanced by the radiative losses (Kang 2011):

$$\tilde{p}_{\text{eq}} = \frac{m_{\text{e}}^2 c v_1}{m_{\text{p}}\sqrt{4e^3q/27}} \left[\frac{B_1}{B_{\text{eff},1}^2 + B_{\text{eff},2}^2}\right]^{1/2}, \qquad (5)$$

where all the quantities except $\tilde{p}_{\text{eq}}$ are expressed in cgs units and the electron equilibrium momentum is normalized as $\tilde{p}_{\text{eq}} = p_{\text{eq}}/m_{\text{p}}c$. Here, $B_{\text{eff}} \equiv (B^2 + B_{\text{CBR}}^2)^{1/2}$ accounts for the loss due to IC scattering of cosmic background photons ($B_{\text{CBR}} = 3.24(1 + z)^2\mu$G) as well as the synchrotron loss. Then, the CR electron spectrum *at the shock location* has the form of $f_{\text{e}}(\tilde{p}) = K_{\text{e/p}} \cdot f_{\text{p}}(\tilde{p}) \cdot \exp\left[-(\tilde{p}/\tilde{p}_{\text{eq}})^2\right]$.

As the primary CR electrons are advected downstream in the postshock region, they also lose energy with the cooling time $t_{\text{rad}} = (0.54\ \text{Gyr})(B_{\text{eff},2}/5\mu\text{G})^{-2}\tilde{p}^{-1}$. This means that the cutoff momentum due to radiative losses decreases with the postshock distance (d) away from the shock front as $\tilde{p}_{\text{cut}}(d) \propto \tilde{p}_{\text{eq}}/d$. As a

result, the downstream, integrated electron spectrum steepens by a power of p as $f_e(\tilde{p}) \propto \tilde{p}^{-(q+1)}$ for $p \geqslant \tilde{p}_{br}$, where the "break" momentum,

$$\tilde{p}_{br} \approx 0.54 \left(\frac{t_{adv}}{1 \text{ Gyr}} \right)^{-1} \left(\frac{B_{eff,2}}{5 \mu G} \right)^{-2}, \quad (6)$$

is the lowest momentum up to which the postshock CR electrons have cooled down. In our simulation sample, a shock is defined as a discontinuity within a grid zone of thickness $\Delta l = 48.8\text{--}195.3 \, h^{-1}$ kpc. The advection time for CR electrons to pass such thickness is $t_{adv} = \Delta l / v_2 \sim 0.1\text{--}0.4$ Gyr for $v_2 \sim 500 \text{ km s}^{-1}$, which is of the order of the dynamical time of typical clusters or the merger time. For the CR electrons emitting at GHz in μG magnetic field ($\tilde{p} \sim 7$), the cooling time becomes shorter than the advection time ($t_{rad}(\tilde{p}) < t_{adv}$), so they have cooled down before exiting the shock zone. Hence, we assume that the *volume-averaged* spectrum of CR electrons within each shock zone has the following form:

$$f_e(\tilde{p})$$
$$= \begin{cases} K_{e/p} \cdot f_{p0} \tilde{p}^{-q} & \text{for } \tilde{p} < \tilde{p}_{br} \\ K_{e/p} \cdot f_{p0} \tilde{p}_{br} \tilde{p}^{-(q+1)} \cdot \exp\left[-\left(\tilde{p}/\tilde{p}_{eq} \right)^2 \right] & \text{for } \tilde{p} > \tilde{p}_{br} \end{cases} \quad (7)$$

Note that we made several assumptions and simplifications, such as the DSA efficiency in Equation (1), the magnetic field strength, B, in Equation (2), the electron-to-proton ratio, $K_{e/p}$, and the volume-averaged electron spectrum in Equation (7).

These modifications will lead to rescaling of synchrotron radiation flux, which may quantitatively affect some of the shock properties in the flux-limited, mock sample of radio relics because a radio relic will consist of multiple shocks in the projected maps (see Section 2.4). However, their impacts on the estimates of derived radio Mach numbers would be marginal, so the main results of this work should remain mostly unaffected (see Section 2.5).

2.4. Mock Radio/X-Ray Maps

We calculate the radio synchrotron emission at shock zones using the magnetic field strength given in Equation (2) and the CR electron spectrum given in Equation (7). For a single electron with $\tilde{p}$, the synchrotron power at frequency ν is given by $P_{\nu,e}(\tilde{p}, \theta) = (\sqrt{3} e^3 B \sin \theta)/(m_e c^2) \times F(\nu/\nu_c)$, where θ is the angle between the electron momentum and magnetic field directions, $\nu_c \equiv 3[(\tilde{p}(m_p/m_e))^2 + 1](eB \sin \theta)/(4\pi m_e c)$ is the characteristic frequency, and $F(x) \equiv x \int_x^\infty d\xi K_{5/3}(\xi)$ ($K_{5/3}(x)$) is modified Bessel function. The synchrotron emissivity (in cgs units of erg cm^{-3} s^{-1} Hz^{-1} str^{-1}) in the shock zone can be estimated as the sum of $P_{\nu,e}$ for all CR electrons of the momentum spectrum $f_e(\tilde{p})$ in the zone, assuming random angular distribution (i.e., $\langle \sin \theta \rangle = \pi/4$),

$$j_\nu = \frac{1}{4\pi} \int_{\tilde{p}_{min}}^\infty \frac{\sqrt{3} \pi e^3 B_2}{4 m_e c^2} F\left(\frac{\nu}{\nu_c(\tilde{p})} \right) f_e(\tilde{p}) d^3\tilde{p}. \quad (8)$$

Note that j_ν is in fact the volume-averaged emissivity because $f_e(\tilde{p})$ in Equation (7) is averaged over the volume of the grid zone, taking account for radiative cooling in the postshock region.

The calculation of the bolometric X-ray emissivity due to thermal bremsstrahlung in the ICM is straightforward and can be done with

$$j_X \approx \left(1.2 \times 10^{-28} \text{ erg cm}^{-3} \text{ s}^{-1} \text{ str}^{-1} \right) T^{1/2} \left(\frac{\rho}{m_p} \right)^2, \quad (9)$$

where the He abundance is assumed to be 7.9% by number (i.e., the mass fractions of $X = 0.76$ and $Y = 0.24$) and the Gaunt factor $g_{ff} \approx 1.2$ for $T > 10^7$ K is used. Note that j_X is calculated at all grid zones, while j_ν is calculated only at shock zones.

Mock radio and X-ray maps of each synthetic cluster are constructed by projecting the synchrotron emissivity, j_ν, and the bolometric X-ray emissivity, j_X, along a depth of $D = 4r_{200}$. The choice of the depth should not affect our results, because both the synchrotron and X-ray emissions beyond r_{200} from the cluster center are, in general, negligible. All lines of sight (LOSs) are assumed to be parallel to one another, because the angular sizes of the observed clusters and radio relics are usually much smaller than one radian. Assuming that the system is optically thin, the synchrotron/X-ray intensities, or surface brightnesses, are calculated by integrating the synchrotron/X-ray emissivities along each LOS (i.e., $I_\nu = \int_{LOS} j_\nu \, dl$ and $I_X = \int_{LOS} j_X \, dl$.).

Because the spatial distribution of shock zones in clusters is quite complicated, they can be translated into radio structures of different morphologies, depending on the projection direction (e.g., Vazza et al. 2012a; Skillman et al. 2013). Thus we choose 24 equally spaced viewing angles for projection, resulting in 24 realizations of radio/X-ray maps for each of 228 synthetic clusters. A total of 5472 radio/X-ray maps were generated and used for the statistics in the following.

Radio telescopes have finite resolutions, so in practice they measure the surface brightness convolved with telescope beams. If a beam has an effective angular area θ^2, then the measured synchrotron flux within the beam is approximately $S_{\nu_{obs}} \approx I_\nu \theta^2 (1 + z)^{-3}$, where $\nu_{obs} = \nu/(1 + z)$ is the redshifted observation frequency. In this study, we adopt $z = 0$ and a beam of $\theta^2 = 15'' \times 15''$ for synthetic radio observation. The beam size is chosen to be comparable to those of future radio surveys, such as those of the Square Kilometre Array (SKA).

Hereafter, we set $\nu_{obs} = 1.4$ GHz as the representative radio frequency, and present $j_{1.4}$ and $S_{1.4}$ at the frequency as radio quantities for synthetic observation. For the calculation of the radio spectral index, two frequencies of 142 MHz and 1.4 GHz are used (see the next subsection).

2.5. "Derived" Mach Numbers

With shocks of different Mach numbers and kinetic energy fluxes existing in clusters as mentioned in introduction, the radio/X-ray structures projected to the sky may consist of shock surfaces of different characteristics. So it may not be straightforward to define the properties for observed structures such as radio relics. In our 3D simulation data cube, each "shock zone" is specified by the sonic Mach number, CR spectrum, and radio emissivity, whereas each zone is assigned with gas density, velocity, temperature, magnetic field strength, and X-ray emissivity, as described in previous subsections. In observations (real or synthetic), on the other hand, the physical properties of shocks must be extracted from 2D projections of

Table 1
Properties of Observed Radio Relics

Source Name	z_{cl}	$P_{1.4}$ (10^{24} W Hz^{-1})	$\langle R \rangle$ (kpc)	l_{LLS} (kpc)	α	References
Abell 2256	0.058	3.95	300	1100	1.2	Clarke & Ensslin (2006)
Abell 1240 N	0.159	0.427	700	650	1.2	Bonafede et al. (2009)
Abell 1240 S	0.159	0.730	1100	1250	1.3	Bonafede et al. (2009)
Abell 2345 E	0.177	2.62	890	1500	1.3	Bonafede et al. (2009)
Abell 2345 W	0.177	2.83	1000	1150	1.5	Bonafede et al. (2009)
Abell 3667	0.056	17.4	1950	1920	1.1	Röttgering et al. (1997)
Abell 548b B	0.042	0.250	430	370	>2.0	Feretti et al. (2006)
Coma 1253+275	0.023	0.284	1940	850	1.18	Giovannini et al. (1991)
Abell 2163	0.203	2.23	1550	450	1.02	Feretti et al. (2004)
Abell S753	0.014	0.205	410	350	2.0	Subrahmanyan et al. (2003)
Abell 115	0.197	16.7	1510	1960	1.1	Govoni et al. (2001)
Abell 610	0.095	0.444	310	330	1.4	Giovannini & Feretti (2000)

radio/X-ray emissivities. Here, we describe the quantification of the sonic Mach number M_s of shocks associated with 2D projected radio/X-ray structures.

We specify the *derived* Mach numbers in two different ways. First, the *weighted* Mach numbers, $M_{1.4}^w$ and M_X^w, are defined as the averages along the LOS, weighted by their synchrotron and X-ray emissivities: $M_{1.4}^w \equiv \int_{LOS} j_{1.4} M_s \, dl / \int_{LOS} j_{1.4} \, dl$ and $M_X^w \equiv \int_{LOS} j_X M_s \, dl / \int_{LOS} j_X \, dl$, respectively. We consider that these weighted Mach numbers represent the true properties of shocks associated with 2D projected structures.

Second, the *observed* Mach numbers, $M_{1.4}^{obs}$ and M_X^{obs}, are designed to mimic the Mach numbers inferred from radio/X-ray observations. In the 2D projected map, a "radio pixel" is the pixel that has at least one shock zone along its LOS and so has $S_\nu > 0$. For each radio pixel, $M_{1.4}^{obs}$ is calculated from the integrated spectral index of synchrotron flux (i.e., $\alpha \equiv -d \ln S_\nu / d \ln \nu = (M_{1.4}^{obs 2} + 1)/(M_{1.4}^{obs 2} - 1)$,) obtained between $\nu_1 = 142$ MHz and $\nu_2 = 1.4$ GHz, following the same way that radio observers usually interpret their observed radio spectra (see Table 1). Note that the value of $M_{1.4}^{obs}$ is not sensitive to the choice of low frequency with our model of CR electron spectrum. However, this practice is only justified only when the break momentum of the volume-integrated electron spectrum is $\tilde{p}_{br} \ll 1$–10 (i.e., when the break frequency in the integrated radio spectrum is $\nu_{br} < 100$ MHz).

For the calculation of M_X^{obs}, the X-ray emission-weighted temperature is calculated along each LOS as $T_X \equiv \int_{LOS} j_X T \, dl / \int_{LOS} j_X \, dl$ in mock maps of clusters. Pixels are tagged as "X-ray shocks," if $|\Delta \log T_X| > 0.11$, as in the shock identification scheme for 3D volume (see Paper I). For X-ray shocks, M_X^{obs} is estimated from the temperature jump (i.e., $T_{X,2}/T_{X,1} = (5M_X^{obs 2} - 1)(M_X^{obs 2} + 3)/(16M_X^{obs 2})$.). The larger of the values of M_X^{obs} estimated along the two primary (x and y) directions on projected maps is assigned to be the observed Mach number: $M_X^{obs} = \max(M_{X,x}^{obs}, M_{X,y}^{obs})$. Again, only X-ray shocks with $M_X^{obs} \geqslant 1.5$ are considered. Note that a pixel identified as an X-ray shock may not be a "radio pixel" and vice versa. In fact, only a small fraction (∼7%) of radio pixels are identified as X-ray shocks. Although the fraction may differ in real observations, this suggests that X-ray observations could miss a substantial fraction of radio shocks. Because it is caused by the smoothing in projection, this problem may be difficult to

be overcome, even if the angular resolution of X-ray observation is improved.

3. PROJECTION EFFECTS ON RADIO/X-RAY MAP

In this section, we examine how the projection affects the radio/X-ray observations of shocks, such as the morphologies and derived shock parameters. As a representative example, we consider a cluster from 100 h^{-1} Mpc box simulation with 2048^3 grid zones. This cluster is identical to the one in the left panels of Figure 1, as well as in Figure 7 of Paper I. It has an X-ray emission-weighted temperature $k_B T_{X,cl} \approx 2.7$ keV and $r_{200} \approx 1.81 \, h^{-1}$ Mpc. The shock that produces the largest amount of CR protons in this cluster is an infall shock with $M_s \approx 5$ and $f_{CR} \approx 1.5 \times 10^{47}$ erg s^{-1} (h^{-1} Mpc)$^{-2}$ (see Paper I).

Figure 1 shows the projected maps of the cluster, viewed from four different angles, zoomed around the area of $r \leqslant r_{200}$ (dashed circle), where r is the distance from the cluster center in the projected plane. Here, the synchrotron flux, $S_{1.4}$, is shown as contours of black solid lines, which is superposed with the bolometric X-ray surface brightness, I_X, in grayscale. The lowest contour level for the synchrotron flux is $S_{1.4,min} = 10^{-2}$ mJy/beam, which could be detected by future radio observatories, such as the SKA. The projection direction of each map is given in terms of polar and azimuthal angles, θ and ϕ, respectively.

The four maps in Figure 1 exhibit morphologies of radio structures that are distinct from one another. For instance, the radio map in the upper-left panel seems to show a paired structure on the opposite side of the cluster, which could be interpreted as radio relics due to a pair of merger shocks. Here, we tag the radio pixels associated with the left structure as "L-relic" (red color), while those associated with the right structure are tagged "R-relic" (green color). In other three panels, if the shock zone with the largest synchrotron contribution along a given LOS belongs to either an L-relic or R-relic, we color the corresponding radio pixel as red or green, respectively. In the upper-right and lower-left panels, elongated radio structures with length $\gtrsim 1$–2 h^{-1} Mpc are composed of both red (L-relic) and green (R-relic) pixels. This illustrates that even a single connected radio structure in the sky may consist of a number of disconnected shock surfaces in the real 3D volume. Thus, it could be misleading if we try to extract the nature of underlying shocks only from the morphology or shock parameters inferred from radio observations. The radio map in the lower-right panel, on the other
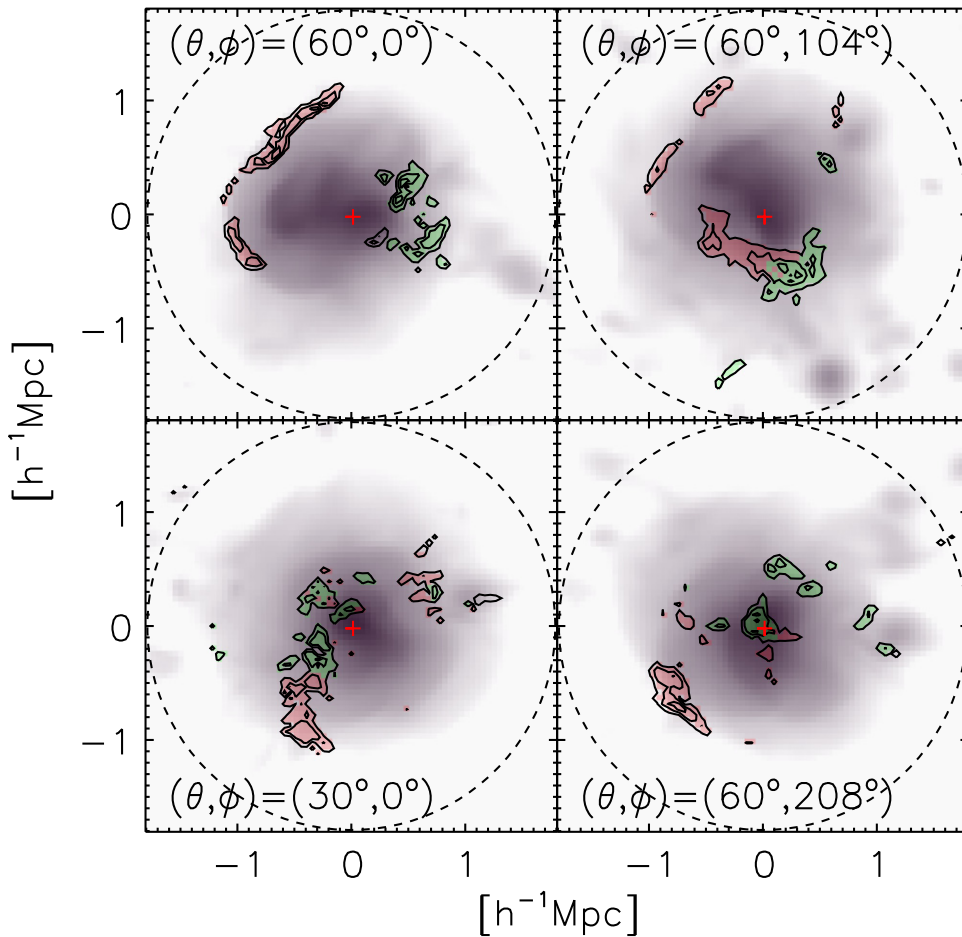
Figure 1. Projected maps of a simulated cluster with $k_B T_{X,\mathrm{cl}} \approx 2.7$ keV at $z = 0$, viewed from four different directions with θ and ϕ listed. Contours show the synchrotron flux at 1.4 GHz, $S_{1.4}$, in logarithmic scale, from 10^{-2} to 1 mJy/beam with an interval of $10^{0.5}$, where a beam of $\theta^2 = 15'' \times 15''$ is adopted. Grayscale maps show the bolometric X-ray surface brightness, I_X, in logarithmic scale, from 10^{-8} (white) to 10^{-2} erg s^{-1} cm^{-2} str^{-1} (black). Dashed circles show r_{200}. Red and green colors differentiate the shock membership associated with the left and right "radio relics," respectively, in the upper-left panel. The red crosses mark the X-ray center of the cluster.

hand, has a number of small structures, and the structure located near the center could be interpreted as a so-called "radio mini-halo" (see, e.g., Brüggen et al. 2012; Feretti et al. 2012, for reviews). Here, we do not intend to address the natures of observed paired structures or halo-like structures in detail, we simply point out that the morphology of observed radio structures critically depends on the projection of underlying 3D structures.

In Figure 2, we compare the spatial distributions of T, ρ, and M_s in a slice (left panels) with those of T_X, $M_{1.4}^{\mathrm{obs}}$, and M_X^{obs} in 2D projection (right panels). The slice passes through $0.37 \, h^{-1}$ Mpc $\sim 0.2 r_{200}$ away from the cluster center, and contains the most radio-luminous shock zones for the L- and R-relics, which are projected at $(-0.4 \, h^{-1}$ Mpc, $1.0 \, h^{-1}$ Mpc$)$ and $(0.4 \, h^{-1}$ Mpc, $0.1 \, h^{-1}$ Mpc$)$ in the 2D maps, respectively. They are identified as infall shocks with $M_s \approx 5.7$ for L-relic and $M_s \approx 3.9$ for R-relic. The right panels are from the same map as that for the upper-left panel of Figure 1, and the contours are drawn with the level of $S_{1.4,\mathrm{min}}$. For $M_{1.4}^{\mathrm{obs}}$, only pixels with $S_{1.4} \geqslant S_{1.4,\mathrm{min}}$ are plotted, while for T_X and M_X^{obs}, only pixels with $I_X \geqslant I_{X,\mathrm{min}} = 10^{-10}$ erg s^{-1} cm^{-2} str^{-1} are plotted. Note that the bolometric X-ray surface brightness in outskirts near the $r \sim r_{200}$ range is typically 1–$10 \times$

10^{-9} erg s^{-1} cm^{-2} str^{-1} in observed clusters (e.g., Ettori & Balestra 2009).

Comparison of M_s in the slice map (bottom left) and $M_{1.4}^{\mathrm{obs}}$ in the 2D map (middle right) indicates that the Mach number and location of shocks with $M_s \gtrsim 3$ agree well in the two distributions, especially for the shocks associated with the L-relic. This is because the radio spectrum in projected maps is governed by one or a few radio-luminous shock zones with high Mach numbers in a given LOS. So $M_{1.4}^{\mathrm{obs}}$ derived from radio observations could be a good proxy for the Mach number of radio-luminous shocks, implying that the properties of such shocks could be extracted reasonably well from radio observations.

On the other hand, there are noticeable differences between the distributions of T/M_s in the slice maps (left-top/bottom) and those of T_X/M_X^{obs} in the 2D maps (right-top/bottom). As seen in top panels, the distribution of T_X is smoother than that of T, partly because the contribution from the X-ray bright ICM dominates over the emissions from the WHIM in surrounding filaments, and also because the projection (integration along LOSs) inevitably irons out any sharp features. The temperature jump across a shock in the T_X map looks reduced. We find that M_X^{obs} derived from X-ray observations tends to underestimate the actual shock Mach number (see the next chapter).
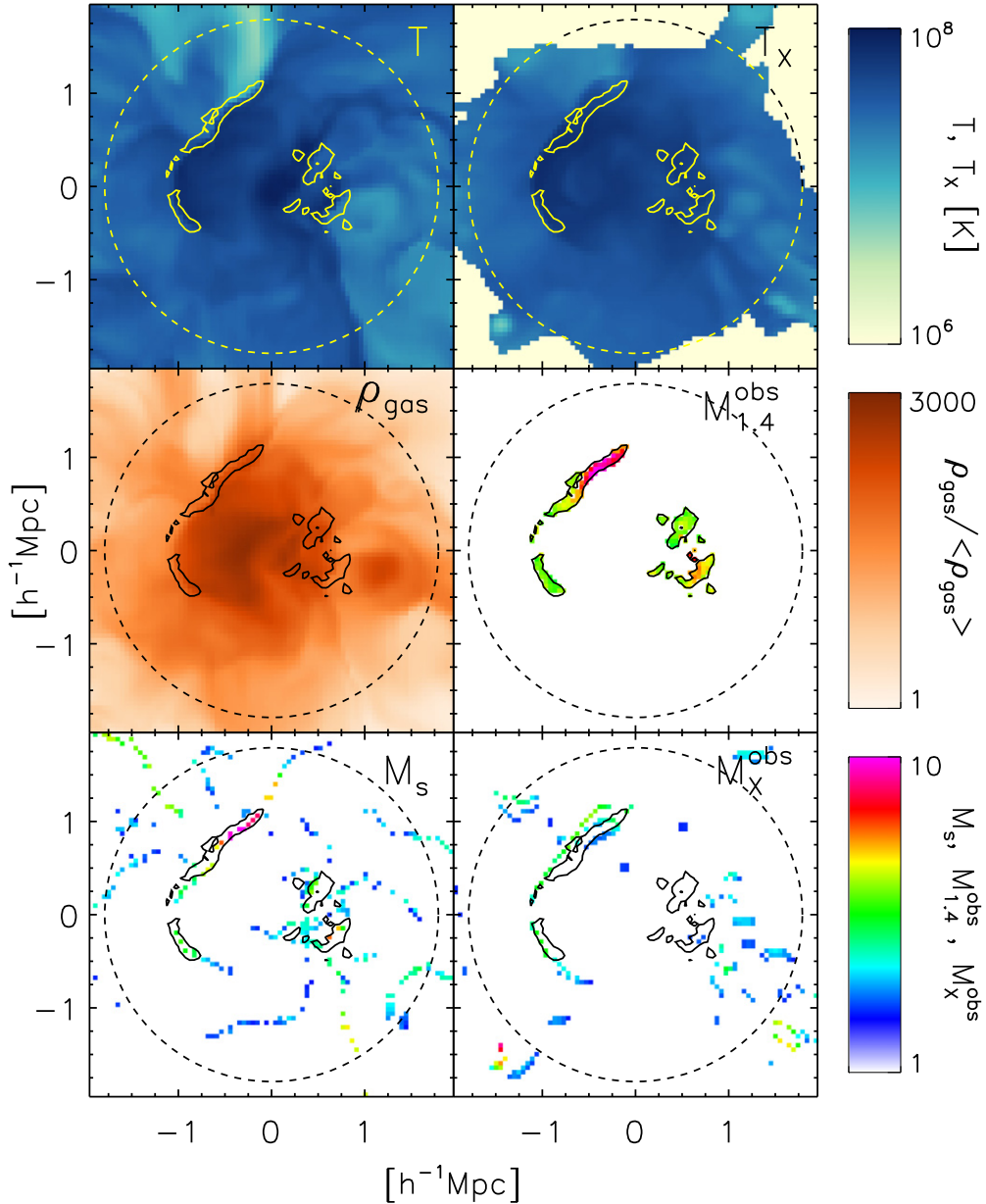
Figure 2. Left panels: distributions of gas temperature T (top), gas density ρ (middle), and shock Mach number M_s (bottom) in a slice that passes through $\sim 0.2 r_{200}$ away from the center of the same cluster as in Figure 1. Right panels: projected maps of X-ray emission-weighted temperature T_X (top), Mach number estimated from the radio spectral index, $M_{1.4}^{obs}$ (middle), and Mach number of X-ray shocks detected in the T_X map, M_X^{obs} (bottom), with the same viewing angle as the upper-left panel of Figure 1. The yellow (top panels) and black (middle and bottom panels) contours correspond to $S_{1.4,min} = 10^{-2}$ mJy/beam. For T_X and M_X^{obs}, the pixels with $I_X \geqslant I_{X,min} = 10^{-10}$ erg s^{-1} cm^{-2} str^{-1} are shown, while for $M_{1.4}^{obs}$, the pixels with $S_{1.4} \geqslant S_{1.4,min}$ are shown. Dashed circles show r_{200}.

We further examine in detail the region near the L-relic, where the slice maps indicate a shock of $M_s \approx 5$–6 formed by the infall of the WHIM along a filament. There is $\sim 100\, h^{-1}$ kpc of positional shift between the locations of shocks in the $M_{1.4}^{obs}$ (middle right) and M_X^{obs} (bottom right) maps. This is because $M_{1.4}^{obs}$ picks up the infall shock, whereas picks up a foreground shock with smaller Mach number formed in the ICM due to the dominant contribution of X-ray from the hot and dense ICM along the LOS (sse below). This may explain spatial offsets between the shock surfaces inferred from radio and X-ray observations in some radio relics (e.g., Akamatsu & Kawahara 2013; Ogrean et al. 2013).

Figure 3 shows the distributions of radio and X-ray emissivities, $j_{1.4}$ and j_X, as functions of M_s for shocks within $r \leqslant r_{200}$ in our simulated clusters. Both distributions have rather large spreads, but the following points are clear. First, j_X decreases with increasing M_s, whereas $j_{1.4}$ increases with M_s, peaks at $M_s \sim 5$, and decreases slightly for higher M_s. These behaviors can be understood as follows: Weaker shocks that tend to form in hot and dense regions near the cluster core produce more j_X, while shocks formed in cluster outskirts with $M_s \sim$ several accelerate CRs and produce $j_{1.4}$ most efficiently. Second, on average, j_X varies over two orders of magnitude, whereas $j_{1.4}$ varies over 10 orders of magnitude. Although both radio/X-ray surface brightnesses on projected maps are dominated by contributions from a small number of bright shock zones along each LOS, the tendency is much stronger in the case of radio.
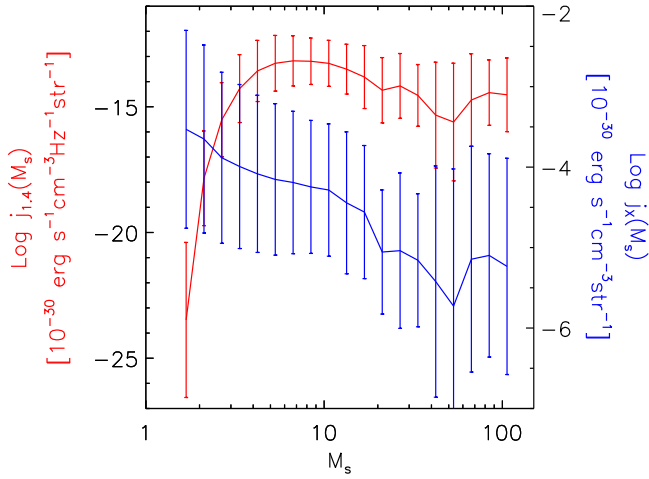
Figure 3. Synchrotron emissivity at 1.4 GHz, $j_{1.4}$, (red) and bolometric X-ray emissivity, j_X, (blue) vs. the Mach number M_s for shock zones within $r \leqslant r_{200}$ from the center in simulated clusters. Connected lines and error bars are averages and standard deviations of $\log j_{1.4}$ and $\log j_X$ within Mach number bins of $[\log M_s, \log M_s + \Delta \log M_s]$.

4. SHOCK PROPERTIES DERIVED FROM RADIO/X-RAY MAPS

4.1. Shock Pixels in Projected Maps

In this section, we first examine the surface brightnesses and derived Mach numbers of pixels with shocks (i.e., $S_{1.4}$, $M_{1.4}$, I_X and M_X) obtained in projected radio/X-ray maps. As noted in Section 2.5, radio pixels that contain shocks in radio maps may not be identified as shocks in X-ray maps, and vice versa. So when we study a correlation between any two quantities, for instance, $M_{1.4}^{\mathrm{obs}}$ versus M_X^{obs}, we use a subset of pixels in which both quantities are specified.

Figure 4 displays the relations between $S_{1.4}$ versus I_X, $M_{1.4}^{\mathrm{obs}}$ versus $S_{1.4}$, and M_X^{obs} versus I_X for pixels within $r \leqslant r_{200}$ from the cluster center. The bottom panel shows that bright X-ray shocks with large I_X tend to be weak with small M_X^{obs}; and the brightest X-ray shocks have $M_X^{\mathrm{obs}} \lesssim 2$. The middle panel, on the other hand, shows that the synchrotron flux $S_{1.4}$ of radio pixels increases with $M_{1.4}^{\mathrm{obs}}$ up to ~ 4 and then decreases for larger $M_{1.4}^{\mathrm{obs}}$. These behaviors should be estimated from those of $j_{1.4}$ and j_X shown in Figure 3. As a result, the correlation between $S_{1.4}$ and I_X turns out to be rather poor, with wide variations in the top panel. What is clear is that the shocks that are brightest in radio are not necessarily brightest in X-ray. In fact, the brightest X-ray shocks have modest radio brightnesses, and vice versa.

Figure 5 displays the relations among mock-observed Mach numbers, $M_{1.4}^{\mathrm{obs}}$ and M_X^{obs}, and weighted Mach numbers, $M_{1.4}^{\mathrm{w}}$ and M_X^{w}, for pixels within $r \leqslant r_{200}$. As noted in the previous chapter, the X-ray Mach numbers tend to be smaller than the radio Mach numbers (upper panels). Again, this is mainly because X-ray observations incline to pick up weaker shocks than radio observations along a given LOS. The correlation between $M_{1.4}$ and M_X is rather poor; the Pearson's linear correlation coefficient of $M_{1.4}^{\mathrm{obs}}$ and M_X^{obs} is $r(\log M_{1.4}^{\mathrm{obs}}, \log M_X^{\mathrm{obs}}) = 0.11$ (upper-left panel) and that of $M_{1.4}^{\mathrm{w}}$ and M_X^{w} is $r(\log M_{1.4}^{\mathrm{w}}, \log M_X^{\mathrm{w}}) = 0.22$ (upper-right panel). So it could be misleading if M_X^{obs} is estimated from $M_{1.4}^{\mathrm{obs}}$, and vice versa. It is expected that there is better
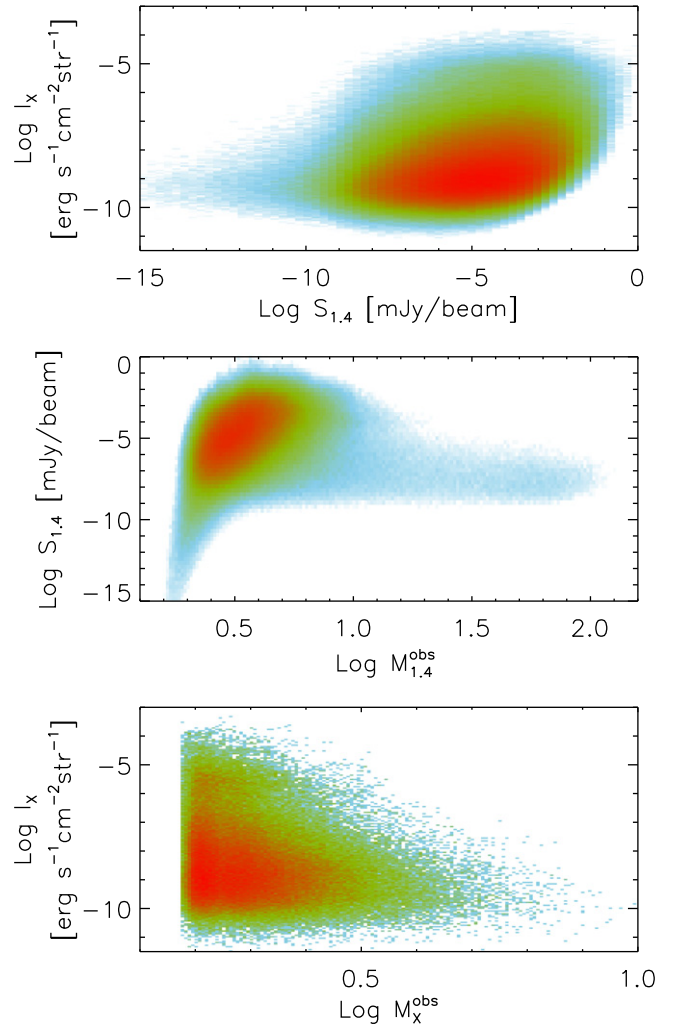

Figure 4. $S_{1.4}$ vs. I_X, $M_{1.4}^{\mathrm{obs}}$ vs. $S_{1.4}$, and M_X^{obs} vs. I_X for shock pixels within $r \leqslant r_{200}$ from the cluster center in projected maps. Here, $S_{1.4}$ is the synchrotron flux at 1.4 GHz, I_X is the bolometric X-ray surface brightness, $M_{1.4}^{\mathrm{obs}}$ is the Mach number estimated from the radio spectral index, and M_X^{obs} is the Mach number of X-ray shocks detected in the T_X map. Colors code the relative frequency, ranging from $10^{-2.5}$ (blue) to 1 (red) in the top and middle panels and from $10^{-3.5}$ (blue) to 1 (red) in the bottom panel.

correlation for M_{obs} and M_{w} of the same band. We find that $M_{1.4}^{\mathrm{obs}}$ is often smaller than $M_{1.4}^{\mathrm{w}}$, as shown in the lower-left panel, but the correlation between them is quite good with $r(\log M_{1.4}^{\mathrm{obs}}, \log M_{1.4}^{\mathrm{w}}) = 0.77$. The correlation between M_X^{obs} and M_X^{w} in the lower-right panel, on the other hand, is still poor with $r(\log M_X^{\mathrm{obs}}, \log M_X^{\mathrm{w}}) = 0.24$. This demonstrates that the smoothing in projection would make the estimation of shock properties harder in X-ray observations than in radio observations.

In Figure 6, we examine the radial distributions of observable properties of shock pixels. Both $M_{1.4}^{\mathrm{obs}}$ and M_X^{obs} tend to increase with radius, and $M_{1.4}^{\mathrm{obs}}$ shows a larger variance than M_X^{obs}. Shocks with an X-ray Mach number of $M_X^{\mathrm{obs}} \gtrsim$ a few would be rare within $r \leqslant r_{200}$, whereas shocks with a radio Mach number of $M_{1.4}^{\mathrm{obs}}$ up to several could be found. Radio bright shocks, for instance, those with $S_{1.4} \geqslant S_{1.4,\mathrm{min}} = 10^{-2}$ mJy/beam, are found mostly in $r \gtrsim 0.2 r_{200}$. This suggests that future radio observations could detect many more shock structures in cluster outskirts. On the
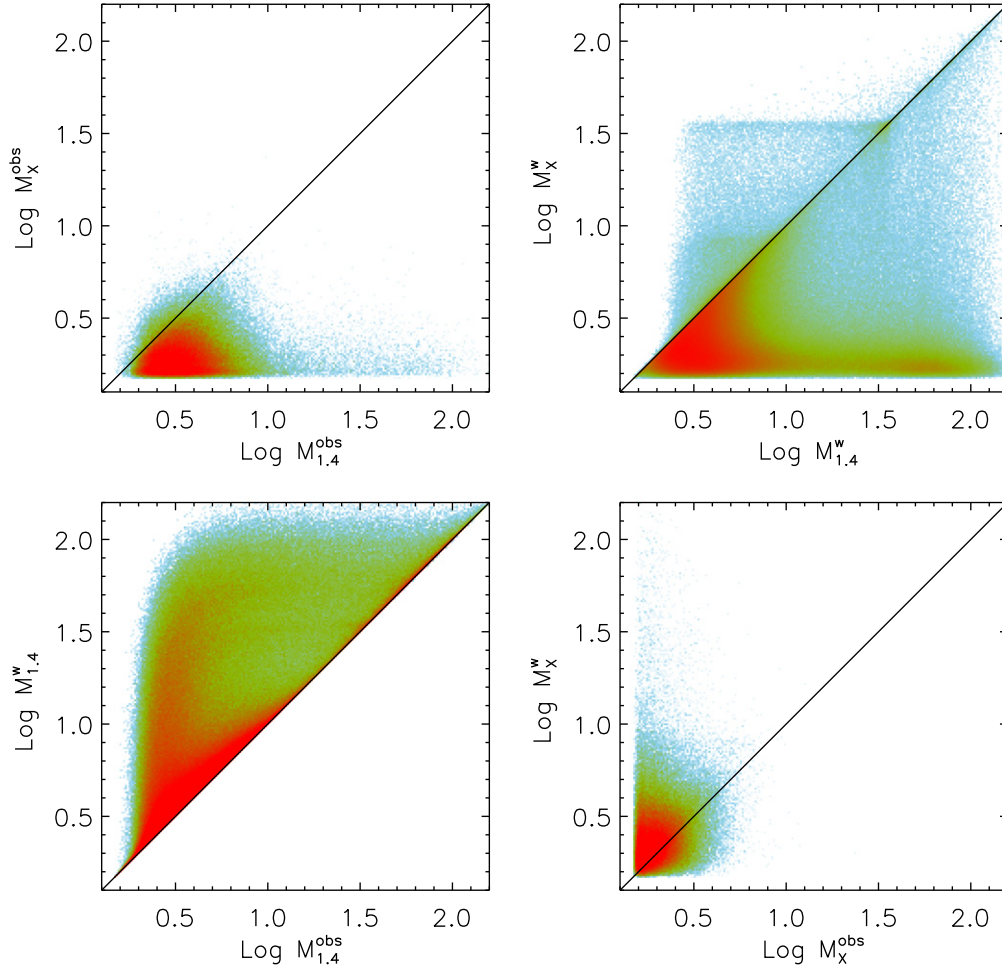
Figure 5. Relations among observed Mach numbers, $M_{1.4}^{obs}$ and M_X^{obs}, and weighted Mach numbers, $M_{1.4}^w$ and M_X^w, (see the text for definitions) for shock pixels within $r \leqslant r_{200}$ from the cluster center in projected maps. Colors code the relative frequency, ranging from $10^{-2.5}$ (blue) to 1 (red) in the upper-left and lower-right panels, from 10^{-4} (blue) to 1 (red) in the upper-right panel, and from 10^{-3} (blue) to 1 (red) in the lower-left panel. Pearson's linear correlation coefficients between two derived Mach numbers at each panel are 0.11 (upper left), 0.22 (upper right), 0.77 (lower left), and 0.24 (lower right). Black lines show the perfection correlation.
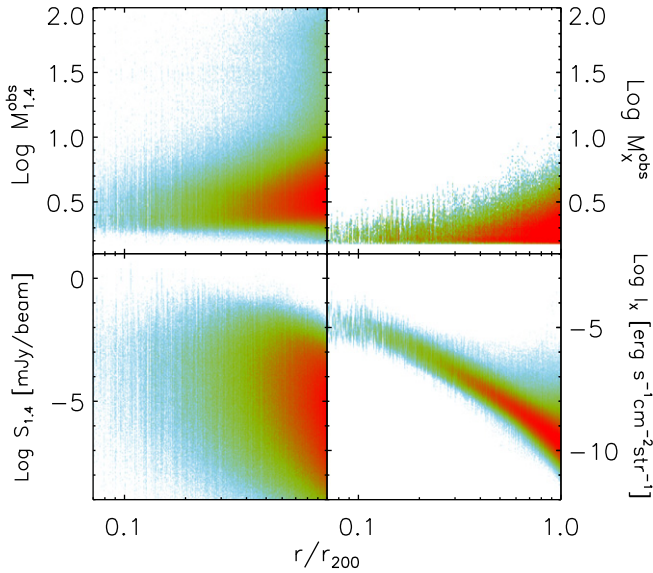

Figure 6. Radial distributions of $M_{1.4}^{obs}$, M_X^{obs}, $S_{1.4}$, and I_X for shock pixels within $r \leqslant r_{200}$ from the cluster center in projected maps. Colors code the relative frequency, ranging from 10^{-3} (blue) to 1 (red) in the left panels, from $10^{-1.5}$ (blue) to 1 (red) in the upper-right panel, and from $10^{-3.5}$ (blue) to 1 (red) in the lower-right panel.

other hand, X-ray bright shocks are preferentially located, and so found close the center. The bolometric X-ray surface brightness of X-ray shocks follows $I_X \propto (r/r_{200})^{-\beta}$ with $\beta \approx$ 3–5 for $r/r_{200} > 0.3$, which is consistent with the observed X-ray profiles in cluster outskirts (e.g., Ettori & Balestra 2009).

4.2. Radio Relics in Projected Maps

We build up a catalog of "synthetic radio relics" by finding connected structures in our radio maps that meet the following conditions: (1) All pixels within structures have $S_{1.4} \geqslant S_{1.4,\text{min}}$. (2) A structure has at least five pixels. Note that the area of a single pixel is $\Delta A = (L/N_g)^2$ (N_g = 1024 or 2048), which means that five pixels corresponds to, for instance, $A_{\min} \approx 0.05$ $(h^{-1}\,\text{Mpc})^2$ in simulations of an $L = 100\,h^{-1}$ Mpc box with 1024^3 grid zones. Using these conditions, we have 9583 radio relic samples: 4626 from simulations of $L = 100\,h^{-1}$ Mpc with 1024^3 grid zones, 4850 from simulations of $L = 200\,h^{-1}$ Mpc with 1024^3 grid zones, and 107 from simulation of $L = 100$ h^{-1} Mpc with 2048^3 grid zones.

We then assign quantities to the synthetic radio relics. The average distance from the cluster center, $\langle R \rangle$, is defined by the synchrotron-weighted average of the distance of the pixels that belong to a radio relic, $\langle R \rangle \equiv \sum_{\text{pixel}} r\, S_{1.4} / \sum_{\text{pixel}} S_{1.4}$, where r
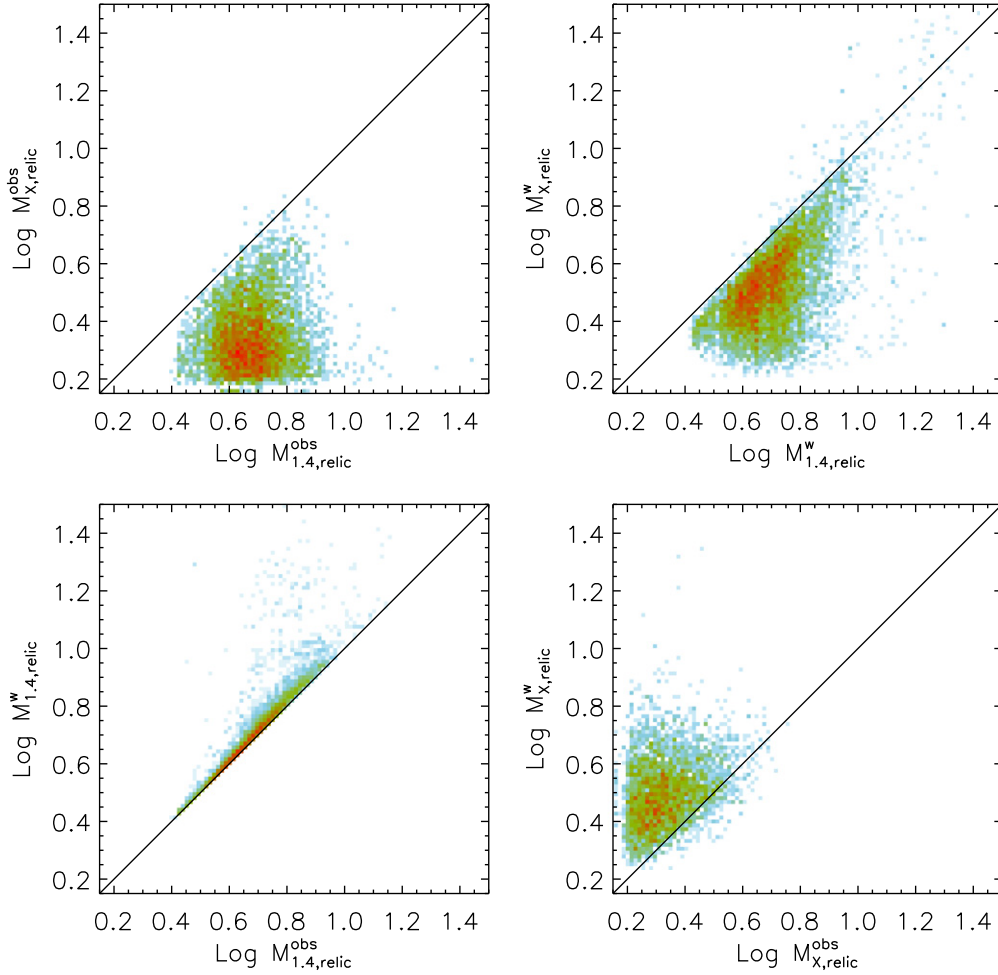
Figure 7. Relations among observed Mach numbers, $M_{1.4,\mathrm{relic}}^{\mathrm{obs}}$ and $M_{X,\mathrm{relic}}^{\mathrm{obs}}$, and weighted Mach numbers, $M_{1.4,\mathrm{relic}}^{\mathrm{w}}$ and $M_{X,\mathrm{relic}}^{\mathrm{w}}$, (see the text for definitions) for synthetic radio relics found within $r \leqslant r_{200}$ from the cluster center in projected maps. Colors code the relative frequency, ranging from 10^{-2} (blue) to 1 (red) in the upper panels, from 10^{-3} (blue) to 1 (red) in the lower-left panel, and from $10^{-1.5}$ (blue) to 1 (red) in the lower-right panel. Pearson's linear correlation coefficients between two derived Mach numbers at each panel are 0.65 (upper left), 0.64 (upper right), 0.99 (lower left), and 0.38 (lower right). Black lines show the perfection correlation.

is the distance of pixels from the cluster center. The derived Mach numbers of radio relics are defined by the synchrotron/ X-ray weighted averages of the corresponding derived Mach numbers of pixels, $M_{1.4}^{\mathrm{obs}}$, $M_{1.4}^{\mathrm{w}}$, M_{X}^{obs}, and M_{X}^{w}. For example, $M_{1.4,\mathrm{relic}}^{\mathrm{obs}} \equiv \sum_{\mathrm{pixel}} M_{1.4}^{\mathrm{obs}} S_{1.4} / \sum_{\mathrm{pixel}} S_{1.4}$ and $M_{X,\mathrm{relic}}^{\mathrm{obs}} \equiv \sum_{\mathrm{pixel}} M_{X}^{\mathrm{obs}} I_X / \sum_{\mathrm{pixel}} I_X$. The number of pixels with M_{X}^{obs} could be smaller than that with $M_{1.4}^{\mathrm{obs}}$, because M_{X}^{obs} is only specified at the pixels identified as X-ray shocks. In fact, about 40% of sample radio relics contain no pixels with M_{X}^{obs}, so the corresponding X-ray Mach number is not assigned to them. The synchrotron power at 1.4 GHz and the bolometric X-ray luminosity of a radio relic are calculated with $P_{1.4} = 4\pi \Delta A \sum_{\mathrm{pixel}} S_{1.4}$ and $L_X = 4\pi \Delta A \sum_{\mathrm{pixel}} I_X$, respectively.

Figure 7 displays the relations among the derived Mach numbers for sample radio relics. The relations follow and look similar to those for pixels in projected maps shown in Figure 5, but the correlations are tighter with $r(\log M_{1.4,\mathrm{relic}}^{\mathrm{obs}}, \log M_{X,\mathrm{relic}}^{\mathrm{obs}})$ $= 0.65$, $r(\log M_{1.4,\mathrm{relic}}^{\mathrm{w}}, \log M_{X,\mathrm{relic}}^{\mathrm{w}}) = 0.64$, $r(\log M_{1.4,\mathrm{relic}}^{\mathrm{obs}}, \log M_{1.4,\mathrm{relic}}^{\mathrm{w}})$ $= 0.99$, and $r(\log M_{X,\mathrm{relic}}^{\mathrm{obs}}, \log M_{X,\mathrm{relic}}^{\mathrm{w}}) = 0.38$. The correlation between $M_{1.4,\mathrm{relic}}^{\mathrm{obs}}$ and $M_{1.4,\mathrm{relic}}^{\mathrm{w}}$ is especially good, indicating that the Mach number estimated from the radio spectral index would be a fair representation of a suitably averaged Mach

number of shocks associated with radio relics. Most of our sample radio relics have $M_{1.4,\mathrm{relic}}^{\mathrm{obs}} \gtrsim 2.5$. This is partly because of the model CR acceleration efficiency we employ (Kang & Ryu 2013), which causes the amount of CR electrons emitting synchrotron to be very small for weak shocks with $M_s \lesssim 2.5$ (see Figure 3 of Paper I). If the CR electron acceleration at weak shocks was more efficient than in our model, radio relics with smaller $M_{1.4,\mathrm{relic}}^{\mathrm{obs}}$ could be more common. As noted in introduction, Merger shocks are expected to have mostly $M_s \lesssim 3$. In fact, we find that our synthetic radio relics normally involve projections of multiple shocks along the LOS, resulting in different morphologies for different viewing angles (see Figure 1). In ~40% of sample radio relics, the brightest pixels with largest $S_{1.4}$ include infall shocks along the LOS, suggesting that infall shocks may account for some radio relics with flat spectra. This seems reasonable in the sense that infall shocks could be the major sources of CRs in clusters, as discussed in Paper I.

Figure 8 displays the radial distributions of $M_{1.4,\mathrm{relic}}^{\mathrm{obs}}$, $M_{X,\mathrm{relic}}^{\mathrm{obs}}$, $P_{1.4}$, and L_X. Upper panels show that most of our synthetic radio relics are found at $\langle R \rangle \gtrsim 0.2 r_{200}$. Although there are wide variations, $M_{1.4,\mathrm{relic}}^{\mathrm{obs}}$ and $M_{X,\mathrm{relic}}^{\mathrm{obs}}$ tend to increase toward outskirts, and on average the radio Mach number is larger than the X-ray Mach number. The lower-left panel shows that
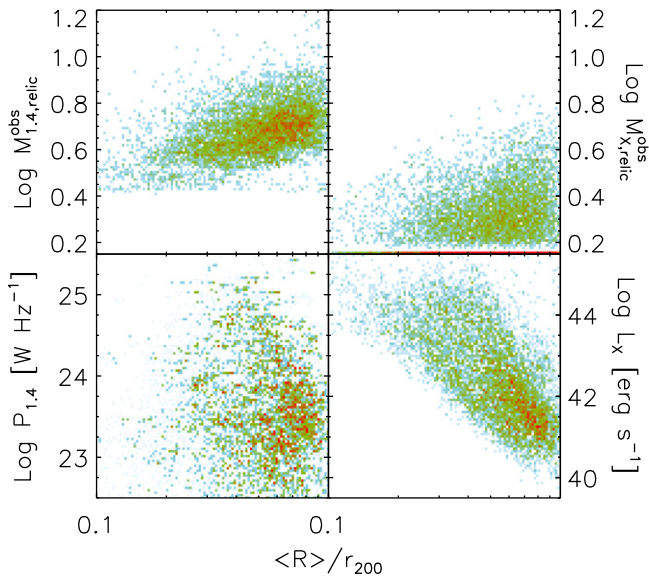
Figure 8. Radial distributions of $M_{1.4,\text{relic}}^{\text{obs}}$, $M_{X,\text{relic}}^{\text{obs}}$, synchrotron power $P_{1.4}$, and bolometric X-ray luminosity L_X for synthetic radio relics found within $r \leqslant r_{200}$ from the cluster center in projected maps. Colors code the relative frequency, ranging from from 10^{-2} (blue) to 1 (red) in the upper panels, from 10^{-1} (blue) to 1 (red) in the lower-left panel, and from $10^{-1.5}$ (blue) to 1 (red) in the lower-right panel.

Figure 9. Synchrotron power $P_{1.4}$ vs. synchrotron-weighted average distance $\langle R \rangle$ and the integrated spectral index α for synthetic radio relics found within $r \leqslant r_{200}$ from the cluster center in projected maps. Filled squares are data points for the observed radio relics listed in Table 1. Colors code the relative frequency, ranging from $10^{-1.5}$ (blue) to 1 (red) in the left panel and from 10^{-2} (blue) to 1 (red) in the right panel.

the radio power at a given radial distance can vary widely, yet most powerful radio relics are found at $0.3 \lesssim \langle R \rangle / r_{200} \lesssim 0.7$. This results mainly from the combined effects of the radial distribution of shock kinetic energy flux and M_s, the strong dependence of CR acceleration efficiency on M_s, and the geometrical increase of relic surface area toward the outskirts (see also Vazza et al. 2012a). The lower-right panel shows a strong radial decline of the bolometric X-ray luminosity of sample radio relics (not including the contributions from the background ICM) toward outskirts. This reflects mostly the radial decreases of gas density and temperature; the effect of the increase of the Mach number and relic surface area is not large here.

4.3. Comparison with Observational Data

We compare our synthetic radio relics with observed radio relics. Table 1 lists the properties of the observed radio relics we use; here, z_{cl} is the redshift of associated clusters, l_{LLS} is the largest linear scale on the sky, and α is the integrated radio spectral index. They are chosen from van Weeren et al. (2009) and Bonafede et al. (2012) with the following criteria: (1) $z_{\text{cl}} \lesssim 0.2$ (our radio relic sample is constructed at $z = 0$), (2) $l_{\text{LLS}} \geqslant A_{\text{min}}^{1/2}$ with $A_{\text{min}} = 0.05(h^{-1}\,\text{Mpc})^2$, and (3) both $P_{1.4}$ and α are available. Note that α in Table 1 was calculated between 74 MHz and 1.4 GHz. Although some observations suggested that the radio spectra of radio relics could have curvatures and α may increase at high frequencies $\gtrsim 10$ GHz (e.g., van Weeren et al. 2009; Stroe et al. 2013; Trasatti et al. 2015), we ignore the effect here.

Figure 9 shows $P_{1.4}$ versus $\langle R \rangle$ and α for synthetic (colors) and observed (filled squares) radio relics. The distribution of $P_{1.4}$ of observed radio relics seems to fall within the range predicted by our synthetic observation. On the other hand, there are noticeable differences in the distributions of $\langle R \rangle$ and α between the synthetic and observed radio relics. First, four
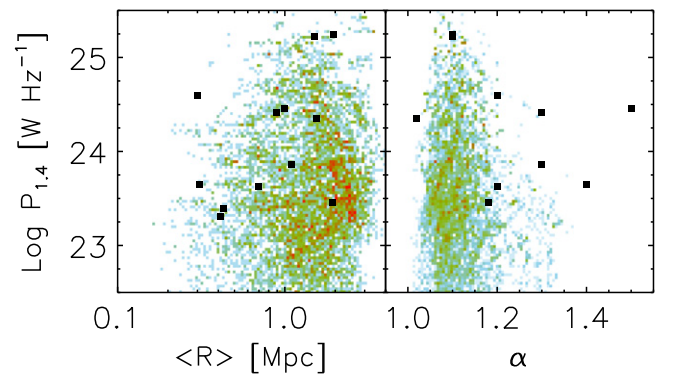
observed radio relics are found with $\langle R \rangle \leqslant 0.43$ Mpc among twelve, while the fraction of synthetic radio relics with $\langle R \rangle \leqslant 0.43$ Mpc is very small, less than $\sim 1\%$. Second, while the integrated spectral index of synthetic radio relics lies $1.0 < \alpha \lesssim 1.38$ (corresponding to $M_s \gtrsim 2.5$), some of the observed radio relics have steeper spectral indices. For example, the radio relics found at Abell 548b B and Abell S753 have $\alpha \gtrsim 2$ ($M_s \lesssim 1.7$), and the radio relic at Abell 2345W has $\alpha \approx 1.5$ ($M_s \approx 2.1$). The discrepancies could be partly because weak shocks close to the cluster core may be under-represented in our structure-formation simulations due to the limited spatial resolution and omission of some non-gravitational processes. But it could be also possible that weak shocks accelerate the CR electrons more efficiently than we assume here, as hinted in recent PIC simulations (see, e.g., Guo et al. 2014; Park et al. 2015).

On the other hand, the re-acceleration of "pre-existing" CR electrons, which is not considered in this study, could play an important role in the production of CR electrons at weak shocks with $M_s \lesssim 2$ (e.g., Kang et al. 2012; Pinzke et al. 2013). Especially, if fossil relativistic electrons are present in the form of isolated clouds, instead of being spread throughout the general ICM space, the relative rareness of radio relics can be understood, as discussed in the introduction (Kang & Ryu 2015; Shimwell et al. 2015). In such a scenario, the "lighting-up" of radio relics is governed mainly by the occasional encounters of ICM shocks with fossil electron clouds, instead of the Mach-number-dependent DSA efficiency and the shock kinetic energy flux. As a result, the frequency and radio luminosity of radio relics may depend less sensitively on the shock Mach number, and much weaker shocks could be turned on as radio relics with steeper spectral index. These features are more consistent with the observational data in Figure 9. Moreover, only a small fraction of ICM shocks become radio sources for the period much shorter than the cluster dynamical timescale (Kang & Ryu 2015). Thus the model naturally explains why radio relics are rare, while structure-formation simulations predict that shocks should be ubiquitous in the ICM (e.g., Ryu et al. 2003; Vazza et al. 2012a). The exploration of this scenario requires extensions of the models we employ here, which is beyond the scope of this paper.

5. SUMMARY

The existence of shocks in clusters of galaxies has been established through observations of radio relics due to synchrotron emission from shock-accelerated CR electrons (e.g., Bonafede et al. 2012), as well as through X-ray observations of shock discontinuities (e.g., Markevitch & Vikhlinin 2007). However, it is not clear whether the properties of shocks inferred from radio and X-ray observations represent their true nature, because we can only measure the quantities projected onto the sky, which are integrated along the LOS. In fact, for a few relics, such as the Tooth brush relic and the radio relic in A2256, radio and X-ray observations have reported inconsistencies in such quantities as shock Mach number and position (Akamatsu & Kawahara 2013; Ogrean et al. 2013; Trasatti et al. 2015).

In this paper, we explored a scenario in which electrons, which are freshly injected and accelerated to high energies via DSA process at the structure-formation shocks, produce radio relics. We constructed synthetic maps of galaxy clusters in radio and X-ray by employing the cosmological hydrodynamic simulation data reported earlier in Paper I. First, the volume-averaged synchrotron emissivity at shock zones was calculated by adopting the CR electron acceleration efficiency based on a DSA model (Kang & Ryu 2013) and magnetic fields based on a turbulent dynamo model (Ryu et al. 2008). The bolometric X-ray emissivity at grid zones was also calculated using the gas density and temperature from simulations. Then, mock maps of the synchrotron and X-ray surface brightnesses in 2D projection were produced by integrating volume emissivities along LOSs for simulated clusters. In the synthetic maps, the properties of shocks and radio relics, such as the shock Mach number and location, were examined in detail.

The main findings can be summarized as follows.

(1) In most cases, radio and X-ray shocks in 2D maps are the outcomes of the projection of multiple shock surfaces along the LOS, because shocks are abundant in the ICM with a mean separation of shock surfaces, $\sim 1\,h^{-1}$ Mpc. As a result, the morphology of shock distributions in 2D maps depends on the projection direction; for the same cluster, very different morphologies may turn out for different viewing angles.

(2) Synchrotron emissivity depends sensitively on the shock Mach number, especially with our DSA model for the CR electron acceleration, while bremsstrahlung emissivity depends on the gas density and temperature. Hence, radio observations tend to pick up shocks of $M_s \sim$ a few to several along a LOS, while X-ray observations preferentially select weaker shocks ($M_s \lesssim 2$) with high density and temperature. Consequently, the properties of shocks in 2D projected maps could be different in radio and X-ray observations. The shock Mach number estimated with X-ray observations tends to be smaller than that from radio observations, if a radio relic consists of multiple shocks along the LOS. In addition, the location of shocks from X-ray observations could be shifted with respect to that from radio observations.

(3) For radio relics, the Mach number estimated from the radio spectral index seems to be a fair representation of the suitably averaged Mach number of the shock surfaces associated with them. On the other hand, the discontinuities in X-ray temperature tend to be smeared due to projection effects, including possible multiple shocks and multiple ICM components, resulting in an X-ray Mach number that is lower than the real Mach number of the associated shock.

(4) When the properties of our synthetic radio relics are compared with those of observed radio relics, there are clear differences in the statistics of radial location and spectral index; more radio relics have been observed closer to the cluster core and with steeper spectral indices than our synthetic observation predicts. This discrepancy may imply that weak shocks in high beta plasmas accelerate CR electrons more efficiently than we model here (see, e.g., Guo et al. 2014; Park et al. 2015). Alternatively, as shown in the previous studies of Kang et al. (2012) and Pinzke et al. (2013), the re-acceleration of pre-existing electrons in the ICM may enhance the production of CR electrons at weak shocks with $M_s \lesssim 2$. Finally, we could also conjecture that radio relics might be activated only when shocks encounter clouds, which contain fossil electrons either accelerated earlier by shocks/turbulence or leftover from old radio jets (see, e.g., Kang & Ryu 2015; Shimwell et al. 2015). This model may explain how very weak shocks can turn on the synchrotron emission, and why radio relics are rare relative to putative shocks in galaxy clusters.

REFERENCES

Akamatsu, H., & Kawahara, H. 2013, PASJ, 65, 16
Akamatsu, H., Takizawa, M., Nakazawa, K., et al. 2012, PASJ, 64, 67
Bagchi, J., Durret, F., Neto, G. B. L., & Paul, S. 2006, Sci, 314, 791
Bell, A. R. 1978, MNRAS, 182, 147
Blandford, R. D., & Ostriker, J. P. 1978, ApJL, 221, L29
Bonafede, A., Brüggen, M., van Weeren, R., et al. 2012, MNRAS, 426, 40
Bonafede, A., Giovannini, G., Feretti, L., Govoni, F., & Murgia, M. 2009, A&A, 494, 429
Bonafede, A., Govoni, F., Feretti, L., et al. 2011, A&A, 530, A24
Brown, S., & Rudnick, L. 2011, MNRAS, 412, 2
Brüggen, M., Bykov, A., Ryu, D., & Röttgering, H. 2012, SSRv, 166, 187
Brunetti, G., & Jones, T. W. 2014, IJMPD, 23, 000
Caprioli, D., Pop, A. R., & Sptikovsky, A. 2015, ApJ, 798, 28
Carilli, C. L., & Taylor, G. B. 2002, ARA&A, 40, 319
Clarke, T. E., & Ensslin, T. A. 2006, AJ, 131, 2900
de Gasperin, F., van Weeren, R. J., Brüggen, M., et al. 2014, MNRAS, 444, 3130
Dolag, K., Bykov, A. M., & Diaferio, A. 2008, SSRv, 134, 311
Drury, L. O. 1983, RPPh, 46, 973
Ensslin, T. A., Biermann, P. L., Klein, U., & Kohle, S. 1998, A&A, 332, 395
Ettori, S., & Balestra, I. 2009, A&A, 496, 343
Feretti, L., Bacchi, M., Slee, O. B., et al. 2006, MNRAS, 368, 544
Feretti, L., Giovannini, G., Govoni, F., & Murgia, M. 2012, A&ARv, 20, 54
Feretti, L., Orrù, E., Brunetti, G., et al. 2004, A&A, 423, 111
Gabici, S., & Blasi, P. 2003, ApJ, 583, 695
Giovannini, G., & Feretti, L. 2000, NewA, 5, 335
Giovannini, G., Feretti, L., & Stanghellini, C. 1991, A&A, 252, 528
Govoni, F., & Feretti, L. 2004, IJMPD, 13, 1549
Govoni, F., Feretti, L., Giovannini, G., et al. 2001, A&A, 376, 803
Guo, X., Sironi, L., & Narayan, R. 2014, ApJ, 797, 47
Hoeft, M., Brüggen, M., Yepes, G., Gottlöber, S., & Schwope, A. 2008, MNRAS, 391, 1511
Hong, S. E., Ryu, D., Kang, H., & Cen, R. 2014, ApJ, 785, 133 (Paper I)
Kang, H. 2011, JKAS, 44, 49
Kang, H. 2015a, JKAS, 48, 9
Kang, H. 2015b, JKAS, 48, 155
Kang, H., Jones, T. W., & Gieseler, U. D. J. 2002, ApJ, 579, 337
Kang, H., Petrosian, V., Ryu, D., & Jones, T. W. 2014, ApJ, 788, 142

Kang, H., & Ryu, D. 2013, ApJ, 764, 95
Kang, H., & Ryu, D. 2015, ApJ, 809, 186
Kang, H., Ryu, D., Cen, R., & Ostriker, J. P. 2007, ApJ, 669, 729
Kang, H., Ryu, D., & Jones, T. W. 2012, ApJ, 756, 97
Malkov, M. A., & Drury, L. O'C. 2001, RPPh, 64, 429
Markevitch, M., Gonzalez, A. H., David, L., et al. 2002, ApJL, 567, L27
Markevitch, M., & Vikhlinin, A. 2007, PhR, 443, 1
Miniati, F., Ryu, D., Kang, H., et al. 2000, ApJ, 542, 608
Morlino, G., Amato, E., & Blasi, P. 2009, MNRAS, 392, 240
Nuza, S. E., Hoeft, M., van Weeren, R. J., Gottlöber, S., & Yepes, G. 2012, MNRAS, 420, 2006
Ogrean, G. A., & Brüggen, M. 2013, MNRAS, 433, 1701
Ogrean, G. A., Brüggen, M., van Weeren, R., et al. 2014, MNRAS, 440, 3416
Ogrean, G. A., Brüggen, M., van Weeren, R. J., et al. 2013, MNRAS, 433, 812
Park, J., Caprioli, D., & Sptikovsky, A. 2015, PhRvL, 114, 085003
Pfrommer, C., & Jones, T. W. 2011, ApJ, 730, 22
Pfrommer, C., Springel, V., Enßlin, T. A., & Jubelgas, M. 2006, MNRAS, 367, 113
Pinzke, A., Oh, S. P., & Pfrommer, C. 2013, MNRAS, 435, 1061
Porter, D. H., Jones, T. W., & Ryu, D. 2015, ApJ, 810, 93
Roettiger, K., Burns, J. O., & Stone, J. M. 1999, ApJ, 518, 603
Röttgering, H. J. A., Wieringa, M. H., Hunstead, R. W., & Ekers, R. D. 1997, MNRAS, 290, 577
Russell, H. R., Sanders, J. S., Fabian, A. C., et al. 2010, MNRAS, 406, 1721
Ryu, D., Kang, H., Cho, J., & Das, S. 2008, Sci, 320, 909
Ryu, D., Kang, H., Hallman, E., & Jones, T. W. 2003, ApJ, 593, 599
Ryu, D., Ostriker, J. P., Kang, H., & Cen, R. 1993, ApJ, 414, 1

Ryu, D., Schleicher, D. R. G., Treumann, R. A., Tsagas, C. G., & Widrow, L. M. 2012, SSRv, 166, 1
Schlickeiser, R. 2002, Cosmic Ray Astrophysics (Berlin: Springer)
Shimwell, T. W., Markevitch, M., Brown, S., Feretti, L., et al. 2015, MNRAS, 449, 1486
Skillman, S. W., O'Shea, B. W., Hallman, E. J., Burns, J. O., & Norman, M. L. 2008, ApJ, 689, 1063
Skillman, S. W., Xu, H., Hallman, E. J., et al. 2013, ApJ, 765, 21
Stroe, A., Harwood, J. J., Hardcastle, M. J., & Röttgering, H. J. A. 2014a, MNRAS, 455, 1213
Stroe, A., Rumsey, C., Harwood, J. J., et al. 2014b, MNRAS, 441, L41
Stroe, A., van Weeren, R. J., Intema, H. T., et al. 2013, A&A, 555, 110
Subrahmanyan, R., Beasley, A. J., Goss, W. M., Golap, K., & Hunstead, R. W. 2003, AJ, 125, 1095
Subramanian, K., Shukurov, A., & Haugen, N. E. L. 2006, MNRAS, 366, 1437
Trasatti, M., Akamatsu, H., Lovisari, L., et al. 2015, A&A, 575, A45
van Weeren, R. J., Röttgering, H. J. A., Brüggen, M., & Cohen, A. 2009, A&A, 508, 75
van Weeren, R. J., Röttgering, H. J. A., Brüggen, M., & Hoeft, M. 2010, Sci, 330, 347
van Weeren, R. J., Röttgering, H. J. A., Intema, H. T., et al. 2012, A&A, 546, A124
Vazza, F., Brüggen, M., van Weeren, R., et al. 2012a, MNRAS, 421, 1868
Vazza, F., Brunetti, G., & Gheller, C. 2009, MNRAS, 395, 1333
Vazza, F., Roediger, E., & Brüggen, M. 2012b, A&A, 544, A103
Widrow, L. M., Ryu, D., Schleicher, D. R. G., et al. 2012, SSRv, 166, 37